# Electronic structure of NdO via slow photoelectron velocity-map imaging spectroscopy of $NdO^-$

Mark C. Babin,[1,#] Martin DeWitt,[1,#] Jessalyn A. DeVine,[1,a] David C. McDonald II,[2] Shaun G. Ard,[3] Nicholas S. Shuman,[3] Albert A. Viggiano,[3,*] Lan Cheng,[4,*] Daniel M. Neumark[1,5,*]

[1] Department of Chemistry, University of California, Berkeley, CA, USA

[2] NRC postdoc at Air Force Research Laboratory, Space Vehicles Directorate, Kirtland Air Force Base, New Mexico 87117, USA

[3] Air Force Research Laboratory, Space Vehicles Directorate, Kirtland Air Force Base, Albuquerque, New Mexico 87117, USA

[4] Department of Chemistry, Johns Hopkins University, Baltimore, Maryland 21218, USA

[5] Chemical Sciences Division, Lawrence Berkeley National Laboratory, Berkeley, CA, USA

[#] These authors contributed equally

[a] Current address: Department of Dynamics at Surfaces, Max-Planck Institute for Biophysical Chemistry, Am Faßberg 11, 37077 Göttingen, Germany

**Corresponding Authors**

[*] lcheng24@jhu.edu, dneumark@berkeley.edu, rvborgmailbox@us.af.mil

## ABSTRACT

Electronically excited NdO is a possible product of the chemistry associated with the release of Nd into the ionosphere, and emission from these states may contribute to the observations following such experiments. To better characterize the energetics and spectroscopy of NdO, we report a combined experimental and theoretical study using slow photoelectron velocity-map imaging spectroscopy of cryogenically cooled $NdO^-$ anions (cryo-SEVI) supplemented by wavefunction-based quantum-chemical calculations. Using cryo-SEVI, we measure the electron affinity of NdO to be 1.0091(7) eV and resolve numerous transitions to low-lying electronic and vibrational states of NdO that are assigned with the aid of the electronic structure calculations. Additionally, temperature-dependent data suggests contributions from the (2)4.5 state of $NdO^-$ residing 2350 $cm^{-1}$ above the ground anion state. Photodetachment to higher-lying excited states of NdO is also reported, which may help clarify observations from prior release experiments.

## I. Introduction

The electron density of the ionosphere, a region of low density plasma in the upper reaches of earth's atmosphere, significantly impacts radio wave propagation, with the potential to reflect, refract, disperse, or absorb radiation dependent upon frequency.[1] The ionosphere is far from static, with predictable seasonal and diurnal variation[2] as well as unpredictable short term turbulence in the electron densities that can lead to a variety of communications issues. These effects have motivated significant research into the causes and dynamics of ionospheric phenomena, such as equatorial plasma bubbles,[3] which are transient regions of reduced plasma density formed near the equator, and sporadic E-layers,[4] transient regions of enhanced electron density formed at lower altitudes than those typically associated with high electron concentrations. There have also been efforts to determine whether artificially produced plasma can prevent or mitigate the impacts of ionospheric variations. To this end, many ionospheric chemical release experiments have been performed, with the released species typically being materials such as barium or cesium that are easily vaporized, have low ionization energies, and have resonant excitations lying within the solar spectrum.[5] This approach is limited to daytime use, as electron production is dependent upon photo-ionization.

In recent years, attention has turned towards a different mechanism for plasma production: chemi-ionization. A range of metals, primarily lanthanides, form metal oxide cations with bond energies that exceed the ionization energy of the neutral oxide such that

$$M + O \rightarrow MO^{+} + e^{-} \quad (1)$$

is energetically allowed and can proceed spontaneously.[6] It follows that the reverse reaction, dissociative recombination of the metal oxide cation, is endothermic and therefore sufficiently slow such that a long lived plasma is possible. The Metal Oxide Space Cloud (MOSC) experiment employed this chemistry by releasing samarium at altitudes where atomic oxygen was the predominant neutral species,[7-11] with Sm chosen as it is the easiest metal to vaporize for which chemi-ionization with atomic oxygen was thought to be exothermic. While previous flight experiments have employed chemical releases, and even chemi-ionization,[12] the diagnostics available in those earlier cases were more limited.

To determine the chemical species formed, the MOSC experiment applied a broad array of diagnostics, including optical spectra from 400 – 900 nm as well as time- and spatially-resolved plasma density measurements via ALTAIR radar. The observed plasma densities produced were well under predicted values. A subsequent re-evaluation of the thermochemistry of Sm plus O chemi-ionization found it to be much less exothermic than previously reported, as this process is nearly thermoneutral[13] and may in fact be slightly endothermic.[14] The lower-than-expected plasma density was thus likely due to a larger-than-predicted occurrence of dissociative recombination of the samarium oxide cation with an electron. The kinetics of chemi-ionization reactions for a variety of lanthanide species were then studied in a flow tube, and samarium was found to stand out with a chemi-ionization rate constant at least an order of magnitude slower than the other lanthanides.[15, 16]

Given the observed slow endothermic chemi-ionization of samarium and the deleterious impact of dissociative recombination on the density of produced plasma, alternative release species must be considered. Unfortunately, the efficiency and exothermicity of (1) are anti-correlated with vapor pressures across the lanthanide series. Balancing these contrasting trends, neodymium retains a moderate vapor pressure while chemi-ionizing at the collisional limit.[15] Furthermore, neodymium chemi-ionization is unambiguously exothermic ($1.76 \pm 0.10$ eV) thereby eliminating any impact of dissociative recombination.[17, 18]

In the late 1980's, the COPE II experiment released both samarium and neodymium, with optical diagnostics limited to standard photography.[12] The experiment took place in daylight such that visible clouds were formed from both releases, pink from samarium and green from neodymium. The pink cloud was observed to follow the magnetic field lines, while the green cloud moved with the neutral winds, leading researchers to conclude that samarium resulted in plasma production while neodymium did not. Considering later laboratory evidence that neodymium chemi-ionizes much more efficiently than samarium, this conclusion appears questionable, and a number of other possible explanations should be explored.

For example, the neodymium may not have been efficiently vaporized; however, it is then difficult to explain the source of the seemingly sharp, green emission. Alternatively, photoionization (instead of chemi-ionization) may have been the dominant process, although this should also have resulted in plasma from both species since the ionization energies are similar. More likely, the observed emissions in the visible spectrum may have been due to the presence of neutral species, while the ionic species emitted exclusively in the ultraviolet. The observation that the samarium emissions moved along the magnetic field lines could have been a result of a steady state between chemi-ionization and dissociative recombination. In this picture, ionic species are dispersed by the magnetic field followed by recombination to yield neutral species along the field lines. The key to resolving this discrepancy lies in the spectroscopy, kinetics, and energetics of the lanthanide oxides and their cations, so that more definitive assignments may be made.

Spectroscopy of the atomic lanthanides is well characterized,[19] but the spectroscopy of the oxides is very much a work in progress.[20, 21] SmO, NdO, and their cations have many low-lying electronic states due to their partially filled *f*-shells and are challenging to explore. Electronic states of $NdO^+$ with term energies of up to ~5,000 $cm^{-1}$ have been determined using pulsed-field ionization zero electron kinetic energy (PFI-ZEKE) spectroscopy.[18] A large number of electronic states of SmO were reported from slow photoelectron velocity-map imaging spectroscopy of cold $SmO^-$ (cryo-SEVI).[22] Previous photoelectron spectra of $NdO^-$ found the electron affinity (EA) of NdO to be 1.01(1) eV,[23] and emission and absorption lines of NdO have been reported in the region between 9500 – 20000 $cm^{-1}$ at modest resolution.[24, 25] A large number of bands at higher resolution were measured lying between 7500 and 12600 $cm^{-1}$,[26] and laser induced fluorescence (LIF) identified low lying states in agreement with ligand field theory.[27, 28] Complete active space self-consistent-field (CASSCF) and multireference configuration interaction (MRCI) calculations detail 54 states below 8000 $cm^{-1}$,[29] amongst a number of theoretical efforts.[30-32]

Here, we utilize slow photoelectron velocity-map imaging spectroscopy of cryogenically cooled $NdO^-$ anions (cryo-SEVI) in tandem with high-level quantum chemical calculations to investigate the electronic and vibrational structure of neutral NdO. The inherent high resolution of SEVI coupled with

the spectral clarity afforded by detachment from cold ions reveals detailed spectroscopic information about $NdO^{0/-}$. We obtain an accurate electron affinity for NdO along with term energies and fundamental vibrational frequencies for several low-lying electronic states of $NdO^{0/-}$. In addition to a wealth of information regarding the neutral's electronic states, manipulation of ion temperature shows evidence of detachment from an excited state of $NdO^-$. Several high-lying excited states of NdO are identified that may explain the green emission observed in Nd releases, though further theoretical work is required to make definitive state assignments.

## II. Experimental Methods

The cryo-SEVI method and instrument have been previously described in detail.[33-35] In this work, $NdO^-$ anions are generated by focusing the frequency-doubled output of a Nd:YAG laser operating at 20 Hz onto a rotating and translating neodymium target. The resulting plasma is entrained within a burst of helium carrier gas from an Even-Lavie pulsed valve,[36] which passes through a narrow clustering channel before expanding into vacuum.

Ions packets then pass through an electrostatic skimmer into a radiofrequency (RF) hexapole ion guide and a RF quadrupole mass filter, which is tuned to ensure that a narrow mass range of ions, encompassing $NdO^-$, are transmitted into the subsequent cryogenically cooled linear RF octupole ion trap. While trapped, ions undergo collisions with a buffer gas mixture of 80:20 He:$H_2$ held at 5 K. After ~40 ms in the trap, ions are assumed to be cooled to their ground vibrational and electronic states. This cooling scheme has been shown to result in molecular temperatures as low as 10 K following extraction from the trap.[35]

The ions are extracted from the trap into an orthogonal Wiley-McLaren time-of-flight mass spectrometer and steered to the laser interaction region inside a velocity-map imaging (VMI) spectrometer. $^{142}Nd^{16}O^-$ ions are photodetached by vertically polarized light from one of two laser configurations based on a tunable dye laser pumped by the second harmonic of a Nd:YAG laser operating at 20 Hz. Photon energies above 3 eV (24200 $cm^{-1}$, 415 nm) are generated by frequency-doubling the light from the dye laser. For photon energies below 1.3 eV (10500 $cm^{-1}$, 950 nm), the dye laser output is focused into a 63 cm

long Raman cell containing 400 psi of $H_2$ and is red-shifted by 4155 $cm^{-1}$ by the $Q_1(1)$ line in the $H_2$ Raman spectrum.[37, 38] The Stokes shifted light is separated from residual dye light and anti-Stokes shifted light by a 900 nm long-pass dichroic mirror and passed through a linear polarizer to ensure the resulting beam is vertically polarized.

Photoelectrons generated in the interaction region are focused with the velocity map imaging (VMI) electrostatic lens[39, 40] onto a position-sensitive detector comprising two chevron-stacked microchannel plates coupled to a phosphor screen.[41] A CCD camera captures photoelectron events on the screen, and their centroids are computed in real time.[42] Electron centroids are accumulated over several thousand experimental cycles to create a single VMI image for each photodetachment wavelength. The angular and radial photoelectron distributions are reconstructed from an accumulated image using the maximum entropy velocity Legendre reconstruction method.[43] The relationship between electron radial position and kinetic energy (eKE) is calibrated by acquiring VMI images of the well-characterized detachment transitions of atomic $O^-$ and $Cl^-$ at several photon energies.[44, 45]

The VMI spectrometer has an approximately constant resolving power, ΔeKE/eKE, yielding the best eKE resolution for slow photoelectrons.[39, 40] Thus, a SEVI spectrum is acquired by first taking an overview spectrum at a relatively high photon energy before tuning the detachment laser to energies just above the features of interest. This procedure results in a collection of high-resolution spectra, each of which spans a narrow energy window. These spectra are concatenated and scaled to match intensities in the overview spectrum, which is less sensitive to variations of the photodetachment cross section with photon energy. Spectra are plotted as a function of electron binding energy (eBE), given by eBE = hν – eKE.

In addition to eKE distributions, cryo-SEVI images contain information about the anisotropy of photodetachment transitions. Such photoelectron angular distributions (PADs) are described by[46]

$$\frac{d\sigma}{d\Omega} = \frac{\sigma_{tot}}{4\pi}[1 + \beta P_2(\cos\theta)],$$

where $\sigma_{tot}$ is the total detachment cross section, $P_2(x)$ is the second-order Legendre polynomial, $\theta$ is the angle of the outgoing photoelectron velocity vector with respect to the laser polarization axis, and $\beta$ is the

anisotropy parameter. The anisotropy parameter, which ranges from -1 (perpendicular detachment) to +2 (parallel detachment), reflects the angular momentum of the detached electron and is thus tied to the electronic character of each photodetachment transition.[47]

## III. Computational Methods

Calculations of the low-lying electronic energy level structures for $NdO^-$ and NdO were carried out to facilitate the assignment of the experimental spectra. The lowest-lying electronic states of $NdO^-$ and NdO originate from the $Nd^+(6s^2 4f^3)O^{2-}$ and $Nd^{2+}(6s^1 4f^3)O^{2-}$ manifolds of electron configurations, respectively. Spin-orbit coupling among the 4*f* electrons dominates the low-lying electronic energy level structures in these two species, similar to the corresponding cation $NdO^+$ that has the $Nd^{3+}(4f^3)O^{2-}$ configuration for its lowest electronic states.[18]

The present calculations use the state-averaged complete active space self-consistent-field (CASSCF) and N-electron valence second-order perturbation theory (NEVPT2) as implemented in the ORCA program package.[48-51] The differences between the NEVPT2 and CASSCF results serve to provide a reasonable estimate of dynamic correlation effects, as is discussed in Section IV. These computations were performed with the Nd 6*s* and 4*f* orbitals in the active spaces, i.e., an active space consisting of five electrons in eight orbitals for $NdO^-$ and four electrons in eight orbitals for NdO. These calculations include 13 quartet states and 13 doublet states for $NdO^-$ and 13 quintet states and 13 triplet states for NdO. Scalar-relativistic effects were taken into account using scalar-relativistic pseudopotentials (PP)[52] and the accompanying QZVP-PP basis sets.[53] Spin-orbit coupling effects were considered using quasidegenerate perturbation theory within the active spaces. These calculations were carried out at the equilibrium bond length of NdO, 1.8 Å.

The local potential energy surfaces around the equilibrium structures for $NdO^-$ and NdO were then computed, yielding equilibrium bond lengths, the NdO adiabatic electron affinity, and vibrational frequencies. Accurate calculations of the electron affinity of NdO as well as the structural properties require high-level treatment of dynamic correlation effects. The CASSCF, NEVPT2, and multireference configuration interaction with Davidson's size-consistency correction (MRCI+Q)[50] calculations for the

vertical detachment energy (VDE) produce a substantial range of VDE values of 1562 $cm^{-1}$, 7138 $cm^{-1}$, and 4192 $cm^{-1}$, respectively. The highest-order method among these multireference approaches, MRCI+Q, lacks size-extensivity and might have difficulty in providing an accurate electron affinity. Instead, we have used scalar-relativistic coupled-cluster singles and doubles augmented with a noniterative triples [CCSD(T)][54] method for the calculations for the ground state properties of $NdO^-$ and NdO. The ground states of $NdO^-$ and NdO both have three unpaired 4*f* electrons occupying the $l_z$=1, 2, and 3 sub-levels. Therefore, we have optimized the high-spin quartet configuration $[4f(l_z=3,m_s=1/2)]^1[4f(l_z=2,m_s=1/2)]^1[4f(l_z=1,m_s=1/2)]^1$ for $NdO^-$ and the high-spin quintet configuration $[6s(m_s=1/2)]^1[4f(l_z=3,m_s=1/2)]^1[4f(l_z=2,m_s=1/2)]^1[4f(l_z=1,m_s=1/2)]^1$ for NdO in the Hartree-Fock calculations.

Note that these two configurations each correspond to a single complex-valued determinant; they consist of more than one single determinant when using real-valued wavefunctions. We thus use a complex-valued Hartree-Fock and CCSD(T) module[55] in the CFOUR program package[56, 57] together with the scalar-relativistic one-electron Hamiltonian integrals of the spin-free exact two-component theory in its one-electron variant (the SFX2C-1e scheme).[58, 59] Correlation-consistent triple-zeta basis sets[60, 61] contracted for the SFX2C-1e scheme (cc-pVTZ-X2C) were used in these CCSD(T) calculations. The SFX2C-1e-CCSD(T) adiabatic electron affinity was augmented with a spin-orbit correction obtained from SO-CASSCF/NEVPT2 calculations.

## IV. Results

### A. Experimental Results

Cryo-SEVI spectra obtained for detachment from $NdO^-$ are presented in Figs. 1 and 2, showing two regions of structure: a low-eBE region between roughly 5500-10500 $cm^{-1}$ (Fig. 1), and a high-eBE region between 15500-28000 $cm^{-1}$ (Fig. 2). Both regions display extensive structure that is well resolved, though the high-eBE region is considerably more congested.

Peak positions and assignments of labeled features in Fig. 1 are reported in Table 1 along with a comparison to our CASSCF computations and term energies determined by rotational analysis of

experimental LIF results by Linton and co-workers.[27] The weak transitions labeled in lowercase in Fig. 1A (a-g) are found to have temperature-dependent intensities, as observed by acquiring spectra under different trapping conditions (Fig. 1B). Spectra were collected at two different buffer gas pressures, differing by a factor of 5, with lower pressures leading to less efficient cooling and warmer ions. As the intensities are higher for detachment from warmer ions, these peaks are assigned to vibrational or electronic hot bands and are discussed further in Section V. The positions of features labeled in Fig. 2 are reported in Table 2 alongside available literature values.[28, 32] In these tables, electronic states are labelled using Hund's case c notation with the ($N$)Ω convention common in the literature on NdO;[20, 27, 28, 62] ($N$)Ω represents the $N^{th}$ state with each value of Ω, the summed projections of the electronic orbital and spin angular momenta onto the internuclear axis. Assignments listed in Table 1 for the peaks with upper case letters originate from the anion ground state (see below) and refer to the neutral states. They include the vibrational transition, denoted as ($v$'-$v$"), where $v$' is the vibrational quanta in the final neutral state and $v$" is the vibrational quanta in the anion.

All features in the low-eBE region (Fig. 1) have PADs that are strongly parallel to the laser polarization ($1 < \beta < 1.8$), in agreement with the conventional PES measurements of Chi and co-workers.[23] Those in Fig. 2 vary – features A1-F1 have PADs aligned weakly parallel to the laser polarization ($-0.1 < \beta < 0.4$), while features lying higher in energy (eBE > 18000 $cm^{-1}$) tend to have PADs slightly perpendicular to the laser polarization ($-0.5 < \beta < 0$).

### B. Computational Results

As shown in Table 3, the computed spectroscopic parameters at the SFX2C-1e-CCSD(T)/cc-pVTZ-X2C level for NdO and $NdO^+$ agree well with previously reported values. The computed adiabatic ionization energy of 44134 $cm^{-1}$ for NdO also compares favorably with the recently measured value of 44427 $cm^{-1}$ by Heaven and collaborators[18] – a value that differed from a previous value[63] by more than 0.5 eV. The excellent agreement thus supports the new measured value and validates the accuracy of the present calculations. Similarly, the computed adiabatic electron affinity of NdO, 8093 $cm^{-1}$, is remarkably

close to our measured value of 8139 $cm^{-1}$, suggesting that this methodology accurately captures the physics of these systems well.

Tables 4 and 5 outline the computed electronic energy level structure for $NdO^{0/-}$ at the CASSCF and NEVPT2 levels of theory. Interestingly, the low-lying electronic states of the neutral NdO are mainly composed of quintet scalar-relativistic wave functions with substantial contributions from the manifold of triplet states, while the contributions to the low-lying electronic states of the anion $NdO^{-}$ are nearly exclusively from the quartet manifold. These computations are in fair agreement with previous MRCI calculations for NdO,[29] and the electronic level structure for $NdO^{-}$ exhibits a similar pattern to that of $NdO^{+}$, which has the same open-shell portion of the electron configuration, $Nd^{2+}(4f^3)$. Further, as the level structure originates from spin-orbit coupling of the 4*f* electrons, the CASSCF calculations within the active space containing the 4*f* electrons captures most of these contributions, with the differences between the NEVPT2 and CASSCF results serving to provide a reasonable estimate of dynamic correlation effects.

Comparison of the computed term energies for these states of NdO with those previously measured by Linton and coworkers[27] finds that our CASSCF results agree more closely with the experimental values than NEVPT2 (see Table 4). Curiously, aside from the (1)5 state, a comparison of the CASSCF term energies to the previously reported values show our calculated energies lie below the measured value by an average of 175 $cm^{-1}$. The inclusion of dynamic correlation in NEVPT2 further reduces the computed values of the term energies, leading to larger deviation from the measured values. A similar underestimation of term energies was also observed in the SO-MRCI calculations previously reported by Heaven and collaborators.[18] Two approximations in the treatment of spin-orbit coupling involved in both the present calculations and those featured in the work of the Heaven group, i.e., the approximation in the construction of the spin-orbit integrals and the neglect of higher-order SO effects, are expected to be responsible for this discrepancy. A further study using more rigorous SO integrals and/or non-perturbative treatment of spin-orbit coupling will be of interest.

A recent ligand field study suggests that higher-lying electronic states of NdO originate from $Nd^{2+}(4f^4)O^{2-}$, $Nd^{2+}(6p^1 4f^3)O^{2-}$, $Nd^{2+}(5d^1 4f^3)O^{2-}$, and $Nd^{2+}(6s^2 4f^2)O^{2-}$ configurations,[32] though one may expect the $Nd^{2+}(6s^2 4f^2)O^{2-}$ configurations to dominate the photodetachment signal via the removal of a single *f* electron from the $Nd^{+}(6s^2 4f^3)O^{2-}$ configurations of $NdO^-$. We thus attempted a CASSCF calculation and a subsequent MRCI+Q calculation for the $Nd^{2+}(6s^2 4f^2)O^{2-}$ configurations with an active space containing two electrons in seven Nd 4*f* orbitals, forcing the 6*s* orbitals to be doubly occupied. Our results from this calculation, however, displayed substantial mixing of the Nd 6*s* orbital with the Nd 5*d* and 4*f* orbitals, suggesting that more complete calculations of these states require the use of an active space comprising the Nd 6*s*, 6*p*, 4*f*, and 5*d* orbitals.

As such, our calculated term energy of 22370 $cm^{-1}$ for the lowest lying state of NdO with the $Nd^{2+}(6s^2 4f^2)O^{2-}$ configuration, $[6s(m_s=1/2)]^2[4f(l_z=3,m_s=1/2)]^1[4f(l_z=2,m_s=1/2)]^1$, appears to be an overestimation, further indicating the need to use a larger active space. The inclusion of Nd 6*s*, 6*p*, 4*f*, and 5*d* orbitals in the active space is beyond our computational resources, so we focus our present discussions of computational results on the lowest-lying states described above.

## V. Discussion

### A. Low-eBE Structure of NdO

Features observed in the low-eBE cryo-SEVI spectra of $NdO^-$ (Fig. 1) are analyzed through comparison with our theoretical results as well as the experimental fluorescence measurements of Linton and co-workers.[27] Features labeled A-G in Fig. 1 are well resolved, representing a significant improvement over the previously reported anion photoelectron spectrum.[23] These features show exceptional agreement with the term energies of NdO determined from the LIF spectra of Linton and coworkers,[27] who identified the corresponding neutral states as belonging to the $\Omega = 4, 5$ manifolds; we thus consider the final neutral states reached in transitions A-G to belong to the same $\Omega = 4, 5$ states. Previous experiments employing photoelectron spectroscopy of lanthanide monoxides[20, 64-67] have shown that photodetachment from a metal-centered 6*s* orbital, as is the case for the $NdO^-$ anion, imposes a $\Delta\Omega = \pm ½$ selection rule. Our results then

strongly suggest detachment from an $NdO^-$ ground electronic state with $\Omega = 4.5$, thus allowing photodetachment transitions to states with $\Omega = 4, 5$. Such transitions are depicted as blue solid lines in Fig. 3 atop an energy level diagram of various electronic and vibrational states of $NdO^{0/-}$ labeled with experimental and calculated energies. This assignment is supported by our CASSCF calculations, which find the (1)4.5 state of $NdO^-$ as the ground state, with the nearest state, (1)3.5, residing 1000 $cm^{-1}$ higher.

Peak A is the lowest-eBE feature whose intensity is not temperature dependent. This, combined with the excellent agreement between the positions of features A-G with the term energies from fluorescence measurements, as well as the spacing of low-lying CASSCF states of NdO, confirms that peak A represents photodetachment to the ground state of neutral NdO. We thus report an electron affinity for NdO of 1.0091(7) eV determined by the eBE of peak A, representing a significant improvement over the previously reported value of 1.01(1) eV,[23] and comparing favorably to our calculated value of 1.0034 eV at the SFX2C-1e-CCSD(T)/cc-pVTZ-X2C level.

Beyond peak A, several features in the cryo-SEVI spectra show evidence of vibrational progressions for different NdO electronic states discussed above. Peaks A-C-F and B-D belong to vibrational progressions in the (1)4 and (1)5 states, respectively, while features E and G correspond to transitions to the next lowest-lying states of NdO in these $\Omega$ manifolds, (2)4 and (2)5, respectively. The spacings within the vibrational progressions A-C-F and B-D yields vibrational frequencies of 828(7) and 831(9) $cm^{-1}$ for the 1(4) and 1(5) states of NdO, respectively. These values are in good agreement with those previously measured in the gas-phase, with Linton and co-workers finding values of 829.512 and 830.218 $cm^{-1}$ for these states, respectively.[27]

These electronic assignments are supported by the PADs measured for the transitions in Fig. 1. The low-lying states of neutral NdO are predicted to differ in electron occupation from those of $NdO^-$ by occupation of the 6*s* orbital, indicating that this is the orbital detached in the lower-eBE spectral region. This orbital is highly localized on the Nd atom; detachment from an atomic *s* orbital yields a photoelectron

angular distribution parallel to the laser polarization,[46] in good agreement with what we observe experimentally for the low-eBE cryo-SEVI spectrum.

### B. Hot bands and structure of $NdO^-$

A number of weak features (a-g) labeled in red in Fig. 1A cannot be explained by previously observed transitions or our calculated transition energies from the (1)4.5 ground state of $NdO^-$. These features are found to have temperature-dependent intensities (Fig. 1B), suggesting they arise from excited states of the anion. To date, the only spectroscopic investigation of $NdO^-$ was performed by Wilson and Andrews, who measured the $NdO^-$ vibrational fundamental as 789.9 $cm^{-1}$ in Ne matrices.[68] As the measured value for the NdO vibrational fundamental is red-shifted by 9 $cm^{-1}$ in Ne matrices compared to the gas-phase,[27, 68] it is reasonable to expect the gas-phase value of the $NdO^-$ fundamental to reside at ~800 $cm^{-1}$, approximately 30 $cm^{-1}$ below that of the neutral.

Based on the expected $NdO^-$ vibrational frequency, we assign features f and g, which reside 36 and 34 $cm^{-1}$ above peaks A and C, respectively, to the (1)4(1-1) and (1)4(2-1) sequence bands for detachment from the (1)4.5 ground state of $NdO^-$. Such an assignment allows for determination of the harmonic vibrational frequency of $NdO^-$ in the ground (1)4.5 state as 792(6) $cm^{-1}$. While excited anion vibrations are not often observed in cryo-SEVI experiments, the good agreement with previous measurements of the anion vibrational frequency bolsters this claim. Further, the presence of these features in cold anions where features a-e are absent suggests these two families of peaks originate from different anionic states.

The remaining hot bands (a-e) cannot be explained by vibrational excitation of $NdO^-$ and prove difficult to conclusively assign due to lack of prior spectroscopic investigations of the electronic states of this anion. We do, however, present one possible assignment of the observed hot bands by drawing on our calculated $NdO^-$ state energies as well as the positions of neutral NdO states identified here and in fluorescence work. In Fig. 1B, black sticks show the eBEs expected for detachment to the NdO state levels calculated from the measurements of Linton and co-workers,[27] where the anion state is considered to be the (2)4.5 excited state of $NdO^-$ with a term energy of 2350 $cm^{-1}$. Detachment from this state follows the same

selection rules as for the (1)4.5 state, resulting in a set of simulated features that can account for features a-e as depicted in Fig. 1B and 3. It should be noted, however, that these simulations also show an expected hot band near 7100 where there is none – this missing transition corresponds to detachment to the $v = 1$ level in the (1)5 excited states of NdO. The intensity of this feature should be much weaker than the corresponding vibrational origin transition for this electronic state, explaining its absence in our spectrum.

The proposed term energy of 2350 $cm^{-1}$ for the (2)4.5 excited state of $NdO^-$ is supported by our CASSCF simulations, which predict such a level to reside 2724 $cm^{-1}$ above the ground state. Further, the presence of anions trapped in low-lying excited states has been observed previously in cryo-SEVI studies,[69-72] though it is notable that the (2)4.5 state of $NdO^-$ lies considerably above the anion ground state, and above 5 other excited states that are not present in the cryo-SEVI spectrum in Fig. 1B. As the buffer gas pressure in these warmer scans is only 20% that of colder scans, it is possible that thermal equilibrium is not achieved in the ion trap at the lower pressure, resulting in ion populations more closely mirroring those from the source.

### C. High-eBE Structure of NdO

The high-eBE structure observed in the cryo-SEVI spectra of $NdO^-$ in Fig. 2 is considerably harder to analyze than the low-eBE structure. The features observed in these spectra correspond to transitions with binding energies ~7000-20000 $cm^{-1}$ above feature A, where there is a significantly higher density of states. The irregularity of peak spacing in this region prevents clear assignment of vibrational progressions.

Prior experimental work is consistent with our measurements – fluorescence work by Linton[27] and Effantin[28] as well as emission spectra from hot $^{142}NdO$ by Shenyavskaya[26] have collectively found states at term energies in the 10500-16500 $cm^{-1}$ range that reside near features observed in the cryo-SEVI spectrum, though state assignments are limited to the value of Ω based on relative intensities of P, Q, and R branches in each transition. These values are reported in the rightmost column of Table 2.

While some features in the cryo-SEVI spectra agree with prior experimental work in this energy regime, it is harder to treat this spectral region theoretically. To date, there are no theoretical studies on excited states of NdO with term energies above 8000 $cm^{-1}$. Given the computational cost of using an active

space with Nd 6*s*, 6*p*, 4*f*, and 5*d* orbitals, our calculations were restricted to an active space consisting of two electrons in seven Nd 4*f* orbitals, forcing a $4f^2 6s^2$ configuration. MRCI+Q calculations using such an active space suggest the term energies for the lowest lying state in this manifold should reside near 22000 $cm^{-1}$, though the failure of this method to reproduce the electron affinity of NdO raises questions about the accuracy of this value.

Nevertheless, some insight into these states can be gleaned from the cryo-SEVI spectra. Detachment from the 4*f* orbital of $NdO^-$ is expected to have a significantly lower cross-section than from the 6*s* orbital,[73] in agreement with the reduced signal intensity observed for transitions in this energy region as compared to the low-eBE cryo-SEVI spectra. Further, the photoelectron angular distributions of features A1-F1 are roughly isotropic, while those of G1-MM are largely perpendicular to the laser polarization, suggesting these manifolds of transitions terminate in states with significantly different orbital occupations. Such an assertion is congruent with recent ligand field theory work that suggest states with term energies greater than 10000 $cm^{-1}$ have $4f^4$ or $4f^3 6p$ configurations (Table 2).[32]

Previous PES studies of lanthanide oxides by the Jarrold group have observed "shake-up transitions" that violate the typical one-electron photodetachment rule, where one electron is detached from the anion while another is promoted, potentially allowing access to states with $4f^4$ or $4f^3 6p$ configurations.[20, 65] This is one possible explanation for some of the features observed in this region of the cryo-SEVI spectrum, particularly peaks CC, J1, L1, and P1, which align with measured transitions involving states with $\Omega \neq 4, 5$ and are thus expected to be forbidden. Such shake-up transitions are expected to be weak, as are the allowed one-electron transitions removing an electron from the 4*f* orbital of NdO, making the distinction between allowed and shake-up transitions challenging.

**Conclusions**

Motivated by Nd release experiments, we have investigated both low- and high-lying excited states of NdO with term energies up to 2000 $cm^{-1}$ and between 10000-20000 $cm^{-1}$ above the ground state, respectively. Observed states agree well with the available literature data, and the lower energy region is

fully assigned to transitions to various vibrational and electronic states of neutral NdO. Further, we report an electron affinity for NdO of 1.0091(7) eV in good agreement with the calculated value at the SFX2C-1e- SFX2C-1e-CCSD(T)/cc-pVTZ-X2C level. CASSCF and NEVPT2 calculations for excited states of $NdO^{0/-}$ agree well with experimental values and support a proposed assignment for a low-lying state of $NdO^{-}$. Transitions in the higher energy states of NdO prove challenging to assign, owing to mixing of the *s* and *f* orbitals in NdO.

Though the current work does provide some insight, further investigation into NdO is needed to ascertain the impact of multiple chemistries during these release experiments, ranging from theoretical exploration of high-lying states of NdO to the oxidation of Nd by molecular $O_2$. Further, while a number of transitions observed in the high-eBE region of the cryo-SEVI spectra have term energies between 18000 and 20000 $cm^{-1}$ (555-500 nm) that may explain the green emission observed during Nd release, increased computational precision for this system is required to determine the states involved and if such transitions are optically allowed.

**Acknowledgments**

The research conducted at UC Berkeley is funded by the Air Force Office of Scientific Research under Grant No. FA9550-19-1-0051, while the work at Johns Hopkins is funded by the Department of Energy, Office of Science, Office of Basic Energy Sciences under Award Number DE-SC0020317, and AFRL work is supported by the Air Force Office of Scientific Research under AFOSR-RV19COR042. M. C. B. thanks the Army Research Office for a National Defense Science and Engineering Graduate fellowship. D.C.M. is supported through the National Research Council Research Associateship Program.

**Data Availability**

The data that support the findings of this study are available from the corresponding author upon reasonable request.

## References:


1. R. Schunk and A. Nagy, *Ionospheres: Physics, Plasma Physics, and Chemistry*. (Cambridge University Press, Cambridge, 2009).
2. D. Bilitza, D. Altadill, Y. Zhang, C. Mertens, V. Truhlik, P. Richards, L.-A. McKinnell and B. Reinisch, J. Space Weather Space Clim. **4**, A07 (2014).
3. H. Kil, L. J. Paxton and S.-J. Oh, Journal of Geophysical Research **114**, A06308 (2009).
4. C. Haldoupis, in *Aeronomy of the Earth's Atmosphere and Ionosphere*, edited by D. P. M. Abdu (Springer, Dordrecht, 2011).
5. N. S. Shuman, D. E. Hunton and A. A. Viggiano, Chem. Rev. **115**, 4542–4570 (2015).
6. K. Schofield, J. Phys. Chem. A **110**, 6938-6947 (2006).
7. P. A. Bernhardt, C. L. Siefring, S. J. Briczinski, A. A. Viggiano, R. G. Caton, T. R. Pedersen, J. M. Holmes, S. G. Ard, N. S. SHuman and K. M. Groves, Radio Science **52**, 559-577 (2017).
8. J. M. Holmes, R. A. Dressler, T. R. Pedersen, R. G. Caton and D. Miller, Radio Science **52**, 521-538 (2017).
9. R. G. Caton, T. R. Pedersen, K. M. Groves, J. Hines, P. S. Cannon, N. Jackson-Booth, R. T. Parris, J. M. Holmes, Y.-J. Su, E. V. Mishin, P. A. Roddy, A. A. Viggiano, N. S. Shuman, S. G. Ard, P. A. Bernhardt, C. L. Siefring, J. Retterer, E. Kudeki and P. M. Reyes, Radio Science **52**, (2017).
10. T. R. Pedersen, R. G. Caton, D. Miller, J. M. Holmes, K. M. Groves and E. Sutton, Radio Science **52**, 578-596 (2017).
11. J. Retterer, K. M. Groves, T. R. Pedersen and R. G. Caton, Radio Science **52**, 604-615 (2017).
12. M. F. Larsen, I. S. Mikkelsen, J. W. Meriwether, R. Niciejewski and K. Vickery, J. Geo. Phys. Res. **94**, 17235-17243 (1989).
13. R. M. Cox, J. Kim, P. B. Armentrout, J. Bartlett, R. A. VanGundy, M. C. Heaven, A. S. G., J. J. Melko, N. S. Shuman and A. A. Viggiano, J. Chem. Phys. **142**, 134307 (2015).
14. M. A. Johnson, (2021).
15. S. G. Ard, N. S. Shuman, O. Martinez Jr., M. T. Brumbach and A. A. Viggiano, J. Chem. Phys. **143**, 204303 (2015).
16. S. G. Ard, N. S. Shuman, O. Martinez Jr, P. Armentrout and A. A. Viggiano, J. Chem. Phys. **145**, 084302 (2016).
17. M. Ghiassee, J. Kim and P. B. Armentrout, J. Chem. Phys. **150**, 144309 (2019).
18. R. A. VanGundy, T. D. Persinger and M. C. Heaven, J. Chem. Phys. **150**, 114302 (2019).
19. A. Kramida, Y. Ralchenko and J. Reader, *NIST Atomic Spectra Database (ver 5.8), [Online]. Available:* http://physics.nist.gov/asd (National Institue of Standards and Technology, Gaithersburg, MD, 2021).
20. J. L. Mason, H. Harb, J. E. Topolski, H. P. Hratchian and C. C. Jarrold, Accounts of Chemical Research **52**, 3265-3273 (2019).
21. Y. Zhou, K. B. Ng, L. Cheng, D. N. Gresh, R. W. Field, J. Ye and E. A. Cornell, J. Mol. Spectrosc. **358**, 1-16 (2019).
22. M. L. Weichman, B. Vlaisavljevich, J. A. DeVine, N. S. Shuman, S. G. Ard, T. Shiozaki, D. M. Neumark and A. A. Viggiano, J. Chem. Phys. **147**, (2017).
23. C. X. Chi, H. Xie, R. Cong, Z. C. Tang and M. F. Zhou, Chinese Journal of Chemical Physics **24**, 604-610 (2011).
24. L. A. Kaledin and E. A. Shenyavskaya, Optika I Spektroskopiya **47**, 1015-1018 (1979).
25. L. A. Kaledin, E. A. Shenyavskaya and I. Kovacs, Acta Physica Hungarica **54**, 189-212 (1983).
26. E. A. Shenyavskaya, A. Bernard and J. Verges, J. Mol. Spectrosc. **222**, 240-247 (2003).
27. C. Linton, C. Effantin, P. Crozet, A. J. Ross, E. A. Shenyavskaya and J. d'Incan, J. Mol. Spectrosc. **225**, 132-144 (2004).
28. C. Effantin, A. Bernard, P. Crozet, A. J. Ross and J. d'Incan, J. Mol. Spectrosc. **231**, 154-164 (2005).
29. A. R. Allouche, M. Aubert-Frecon and S. Y. Umanskiy, J. Chem. Phys. **124**, 184317 (2006).

30. M. Krauss and W. J. Stevens, Molecular Physics **101**, 125-130 (2003).
31. Z. J. Wu, W. Guan, J. Meng and Z. M. Su, Journal of Cluster Science **18**, 444-458 (2007).
32. L. A. Kaledin, J. Mol. Spectrosc. **365**, 111207 (2019).
33. A. Osterwalder, M. J. Nee, J. Zhou and D. M. Neumark, J. Chem. Phys. **121**, 6317-6322 (2004).
34. D. M. Neumark, J. Phys. Chem. A **112**, 13287-13301 (2008).
35. C. Hock, J. B. Kim, M. L. Weichman, T. I. Yacovitch and D. M. Neumark, J. Chem. Phys. **137**, 6 (2012).
36. U. Even, J. Jortner, D. Noy, N. Lavie and C. Cossart-Magos, J. Chem. Phys. **112**, 8068-8071 (2000).
37. D. K. Veirs and G. M. Rosenblatt, J. Mol. Spectrosc. **121**, 401-419 (1987).
38. J. A. DeVine, A. Abou Taka, M. C. Babin, M. L. Weichman, H. P. Hratchian and D. M. Neumark, J. Chem. Phys. **148**, 10 (2018).
39. A. Eppink and D. H. Parker, Rev. Sci. Instrum. **68**, 3477-3484 (1997).
40. M. L. Weichman, J. A. DeVine, D. S. Levine, J. B. Kim and D. M. Neumark, PNAS **113**, 1698-1705 (2016).
41. D. W. Chandler and P. L. Houston, J. Chem. Phys. **87**, 1445-1447 (1987).
42. C. A. M. B. Doyle, and A. G. Suits.
43. B. Dick, Phys. Chem. Chem. Phys. **16**, 570-580 (2014).
44. U. Berzinsh, M. Gustafsson, D. Hanstorp, A. Klinkmuller, U. Ljungblad and A. M. Martenssonpendrill, Phys. Rev. A **51**, 231-238 (1995).
45. C. Blondel, W. Chaibi, C. Delsart, C. Drag, F. Goldfarb and S. Kroger, Eur. Phys. J. D **33**, 335-342 (2005).
46. J. Cooper and R. N. Zare, J. Chem. Phys. **48**, 942-943 (1968).
47. A. Sanov, Annu Rev Phys Chem **65**, 341-363 (2014).
48. C. Angeli, R. Cimiraglia, S. Evangelisti, T. Leininger and J. P. Malrieu, J. Chem. Phys. **114**, 10252-10264 (2001).
49. I. Schapiro, K. Sivalingam and F. Neese, J. Chem. Theory Comput. **9**, 3567-3580 (2013).
50. S. R. Yost and M. Head-Gordon, J. Chem. Phys. **145**, (2016).
51. F. Neese, Wires Comput Mol Sci **8**, (2018).
52. M. Dolg, H. Stoll and H. Preuss, J. Chem. Phys. **90**, 1730-1734 (1989).
53. F. Weigend and R. Ahlrichs, Phys. Chem. Chem. Phys. **7**, 3297-3305 (2005).
54. K. Raghavachari, G. W. Trucks, J. A. Pople and M. Head-Gordon, Chem. Phys. Lett. **589**, 37-40 (2013).
55. J. Z. Liu, Y. Shen, A. Asthana and L. Cheng, J. Chem. Phys. **148**, (2018).
56. D. A. Matthews, L. Cheng, M. E. Harding, F. Lipparini, S. Stopkowicz, T. C. Jagau, P. G. Szalay, J. Gauss and J. F. Stanton, J. Chem. Phys. **152**, (2020).
57. J. G. J.F. Stanton, L. Cheng, M.E. Harding, D.A. Matthews, P.G. Szalay.
58. K. G. Dyall, J. Chem. Phys. **106**, 9618-9626 (1997).
59. W. J. Liu and D. L. Peng, J. Chem. Phys. **131**, (2009).
60. T. H. Dunning, J. Chem. Phys. **90**, 1007-1023 (1989).
61. Q. Lu and K. A. Peterson, J. Chem. Phys. **145**, (2016).
62. P. Carette and A. Hocquet, J. Mol. Spectrosc. **131**, 301-324 (1988).
63. R. J. Ackermann, E. G. Rauh and R. J. Thorn, J. Chem. Phys. **65**, 1027-1031 (1976).
64. J. O. Kafader, J. E. Topolski, V. Marrero-Colon, S. S. Iyengar and C. C. Jarrold, J. Chem. Phys. **146**, (2017).
65. J. O. Kafader, M. Ray and C. C. Jarrold, J. Chem. Phys. **143**, (2015).
66. M. Ray, J. A. Felton, J. O. Kafader, J. E. Topolski and C. C. Jarrold, J. Chem. Phys. **142**, (2015).
67. J. L. Mason, H. Harb, A. Abou Taka, A. J. McMahon, C. D. Huizenga, H. Corzo, H. P. Hratchian and C. C. Jarrold, J. Phys. Chem. A **125**, 857-866 (2021).
68. S. P. Willson and L. Andrews, J. Phys. Chem. A **103**, 3171-3183 (1999).

69. J. B. Kim, M. L. Weichman and D. M. Neumark, Journal of the American Chemical Society **136**, 7159-7168 (2014).
70. J. A. DeVine, M. C. Babin and D. M. Neumark, Faraday Discussions **217**, 235-255 (2019).
71. A. Abou Taka, M. C. Babin, X. H. Sheng, J. A. DeVine, D. M. Neumark and H. P. Hratchian, J. Chem. Phys. **153**, (2020).
72. M. C. Babin, M. DeWitt, M. L. Weichman, J. A. DeVine and D. M. Neumark, Molecular Physics **119**, (2021).
73. J. Felton, M. Ray and C. C. Jarrold, Phys. Rev. A **89**, (2014).

Table 1. Peak positions, shifts from peak A, assignments, and calculated transition energies (CASSCF) for transitions in the low-eBE cryo-SEVI spectra of $NdO^-$ given in Fig 1A are reported in units of $cm^{-1}$. Cryo-SEVI values are compared to values previously reported for a rotational analysis of the NdO LIF spectrum.[27] Transitions labeled in lowercase have increasing intensity with increasing temperature (see Fig. 1B) and are therefore assigned as hot bands. Uncertainties in peak positions correspond to one standard deviation obtained from a Gaussian fit to the high-resolution scan of the experimental peak.

| Peak | eBE | Shift | Assignment | CASSCF | Fluorescence |
|---|---|---|---|---|---|
| a | 5658(28) | -2481 | - | - | - |
| b | 6295(27) | -1844 | - | - | - |
| c | 6594(35) | -1545 | - | - | - |
| d | 7416(35) | -723 | - | - | - |
| e | 7834(15) | -305 | - | - | - |
| A | 8139(6) | 0 | (1)4 (0-0) | 0 | - |
| f | 8175(11) | 36 | (1)4 (1-1) | - | - |
| B | 8614(8) | 475 | (1)5 (0-0) | 529 | 473.691 |
| C | 8967(8) | 828 | (1)4 (1-0) | 831 | 829.512 |
| g | 9000(8) | 862 | (1)4 (2-1) | - | - |
| D | 9445(9) | 1307 | (1)5 (1-0) | 1356 | 1303.909 |
| E | 9735(11) | 1596 | (2)4 (0-0) | 1401 | 1587.241 |
| F | 9797(11) | 1658 | (1)4 (2-0) | - | 1654.453 |
| G | 10293(6) | 2155 | (2)5 (0-0) | 2084 | 2152.575 |

Table 2. Peak positions for transitions in the high-eBE cryo-SEVI spectra of $NdO^-$ given in Fig 3. Cryo-SEVI values are compared to relevant term energies determined for states observed in the LIF measurements of Effantin and co-workers[28]. Electron configurations determined by Kaledin via ligand field theory are reported.[32] All values are reported in $cm^{-1}$.

| Peak | eBE | Shift | Configuration | Fluorescence |
|---|---|---|---|---|
| A1 | 15515 | 7376 | | |
| B1 | 15611 | 7472 | | |
| C1 | 15827 | 7688 | | |
| D1 | 16608 | 8469 | | |
| E1 | 17008 | 8869 | | |
| F1 | 17375 | 9236 | | |
| G1 | 17990 | 9851 | | |
| H1 | 18203 | 10064 | | |
| I1 | 18325 | 10186 | | |
| J1 | 18688 | 10549 | $4f^4$ | 10506.031 |
| K1 | 19423 | 11284 | | |
| L1 | 19663 | 11524 | $4f^4$ | 11539.894 |
| M1 | 19820 | 11681 | $4f^4$ | 11699.061 |
| N1 | 20441 | 12302 | | |
| O1 | 20855 | 12716 | | |
| P1 | 20997 | 12858 | $4f^4$ | 12839.70 |
| Q1 | 21364 | 13225 | | |
| R1 | 21660 | 13521 | | |
| S1 | 22207 | 14068 | $4f^3 6p$ | 14081.326 |
| T1 | 22484 | 14345 | | |
| SU1 | 22780 | 14641 | | |
| V1 | 23099 | 14960 | $4f^4$ | 14969.569 |
| W1 | 23434 | 15295 | | |
| X1 | 23726 | 15587 | | |
| Y1 | 23784 | 15645 | $4f^3 6p$ | 15625.07 |
| Z1 | 24314 | 16175 | $4f^3 6p$ | 16168.376 |
| AA | 24348 | 16209 | | |
| BB | 24542 | 16403 | | 16397.252 |
| CC | 24884 | 16746 | $4f^3 6p$ | 16737.93 |
| DD | 26211 | 18072 | | |
| EE | 26639 | 18500 | | |
| FF | 26792 | 18653 | | |
| GG | 26924 | 18785 | | |
| HH | 27112 | 18973 | | |
| II | 27248 | 19109 | | |
| JJ | 27367 | 19228 | | |
| KK | 27442 | 19303 | | |

| | | |
|---|---|---|
| LL | 27688 | 19549 |
| MM | 27820 | 19681 |

Table 3. Spectroscopic parameters for $NdO^+$, NdO, and $NdO^-$. The "theory" values have been obtained from SFX2C-1e-CCSD(T)/cc-pVTZ-X2C calculations as described in the text. The values of adiabatic ionization energy (IE) and adiabatic electron affinity (EA) have included SO-CASSCF/NEVPT2 spin-orbit coupling corrections of -28 $cm^{-1}$ for IE and 315 $cm^{-1}$ for EA. The experimental values for $NdO^+$ are taken from the work of Heaven and coworkers,[18] the experimental bond length of NdO is the $R_0$ value from Effantin and coworkers,[28] and the $\omega_e$ and $\omega_e\chi_e$ values are derived using the vibrational energy spacings determined by Linton and coworkers.[27]

| | $NdO^-$ | | NdO | | $NdO^+$ | |
|---|---|---|---|---|---|---|
| | Theory | Experiment | Theory | Experiment | Theory | Experiment |
| $R_e$ (Å) | 1.837 | - | 1.800 | 1.801 | 1.754 | 1.74 |
| $\omega_e$ ($cm^{-1}$) | 780 | 792(6) | 835 | 834.1 | 901 | 892.4 |
| $\omega_e\chi_e$ ($cm^{-1}$) | 2.2 | - | 2.1 | 2.3 | 2.1 | 1.3 |
| $EA_a$ ($cm^{-1}$) | - | - | 8093 | 8139 | - | - |
| $IE_a$ ($cm^{-1}$) | - | - | 44134 | 44427 | - | - |

Table 4. Computed levels of NdO from both CASSCF and NEVPT2, both using QZVP-PP basis sets with perturbative inclusion of spin-orbit coupling, along with state assignments, a comparison to experimental fluorescence measurements from Linton and co-workers,[27] and compositions in terms of the spin-free wave functions. Relative energetics are given in $cm^{-1}$ with respect of the ground state of neutral NdO. "(m)n" refers to the m-th electronic state with $\Omega = n$.

| State | CASSCF | NEVPT2 | Measured | Composition |
|---|---|---|---|---|
| (1)4 | 0 | 0 | - | 90% $^5$I + 8% $^5$H |
| (1)5 | 529 | 411 | 473.691 | 45% $^5$I + 42% $^3$I +9%$^5$H +3%$^3$H |
| (1)3 | 934 | 921 | 1156.005 | 60% $^5$H + 28% $^5\Gamma$ +9%$^5\Phi$ |
| (1)2 | 1123 | 1123 | 1351.1 | 37% $^5\Phi$ + 34% $^5\Gamma$ +21%$^5\Delta$ + 7%$^5\Pi$ |
| (1)1 | 1191 | 1188 | - | 33% $^5\Delta$ + 30% $^5\Pi$ + 22% $^5\Phi$ + 14% $^5\Sigma$ |
| (1)$0^+$ | 1225 | 1232 | - | 49% $^5\Pi$ + 31% $^3\Sigma$ + 21%$^5\Delta$ |
| (2)4 | 1401 | 1304 | 1587.241 | 27%$^3$H +27%$^5$H +25%$^5\Gamma$+9%$^5\Phi$+7%$^3\Gamma$ |
| (2)3 | 1600 | 1503 | 1793.2 | 23%$^5\Phi$+21%$^3\Gamma$+18%$^5\Delta$+15%$^5$H +11%$^3\Phi$+5%$^5\Gamma$+5%$^5\Pi$ |
| (2)2 | 1698 | 1602 | 1914.2 | 23% $^5\Gamma$ + 19% $^5\Pi$ + 18% $^3\Phi$ + 15%$^3\Delta$ + 12%$^5\Delta$ + 9% $^5\Sigma$ |
| (2)1 | 1742 | 1648 | - | 19% $^5\Sigma$ + 22% $^5\Phi$ + 19% $^5\Pi$ + 14%$^3\Delta$ + 6%$^3\Sigma$ + 16% $^3\Pi$ |
| (1)$0^-$ | 1753 | 1670 | - | 41% $^5\Delta$ + 24% $^5\Pi$ + 16% $^3\Sigma$ + 19%$^3\Pi$ |
| (1)6 | 2014 | 1946 | 2123.875 | 61%$^5$I +12%$^5$H +24%$^3$I |
| (2)5 | 2084 | 1960 | 2152.575 | 42%$^5$I +3%$^5$H +47%$^3$I +7%$^3$H |
| (3)5 | 2742 | 2683 | - | 32%$^5\Gamma$+4%$^5$I +7%$^5\Phi$+33%$^5$H +3%$^3\Gamma$+4%$^3$I+13%$^3$H |

Table 5. Relative energies ($cm^{-1}$) of the lowest spin-orbit states for $NdO^-$ obtained from CASSCF and NEVPT2 calculations using QZVP-PP basis sets with the perturbative inclusion of spin-orbit coupling, together with compositions in terms of the spin-free wave functions. "(m)n" refers to the m-th electronic state with $\Omega = n$.

| State | CASSCF | NEVPT2 | Composition |
|---|---|---|---|
| (1)4.5 | 0 | 0 | 88% $^4I$ + 9% $^4H$ |
| (1)3.5 | 1000 | 1000 | 28% $^4\Gamma$ + 61% $^4H$ +8%$^4\Phi$ |
| (1)2.5 | 1135 | 1121 | 41% $^4\Gamma$ + 16% $^4\Delta$ +37%$^4\Phi$ |
| (1)1.5 | 1206 | 1178 | 39% $^4\Delta$ + 31% $^4\Phi$ +19%$^4\Pi$ |
| (1)0.5 | 1284 | 1257 | 20%$^4\Delta$+29%$^4\Sigma$+47%$^4\Pi$ |
| (1)5.5 | 1898 | 1920 | 86% $^4I$ + 12% $^4H$ |
| (2)4.5 | 2724 | 2750 | 9%$^4I$ +34%$^4\Gamma$+50%$^4H$ +7%$^4\Phi$ |
| (2)3.5 | 2929 | 2939 | 40%$^4\Phi$+29%$^4H$ +15%$^4\Delta$+15%$^4\Gamma$ |
| (2)2.5 | 3040 | 3056 | 40% $^4\Gamma$ + 35% $^4\Delta$ + 22% $^4\Pi$ |
| (2)1.5 | 3097 | 3094 | 42% $^4\Phi$ + 30% $^4\Sigma$ + 27% $^4\Pi$ |
| (2)0.5 | 3118 | 3120 | 42%$^4\Pi$+41%$^4\Delta$+16%$^4\Sigma$ |
| (1)6.5 | 3907 | 3942 | 91% $^4I$ + 9% $^4H$ |
| (2)5.5 | 4729 | 4771 | 58%$^4H$ +29%$^4\Gamma$+12%$^4I$ |
| (3)4.5 | 4954 | 4983 | 43%$^4\Phi$+34%$^4H$ +21%$^4\Gamma$ |
| (3)3.5 | 5064 | 5098 | 46%$^4\Delta$+41%$^4\Gamma$+8%$^4H$ +5%$^4\Phi$ |
| (3)2.5 | 5131 | 5149 | 46% $^4\Pi$ + 38% $^4\Delta$ + 15% $^4\Gamma$ |
| (3)1.5 | 5173 | 5188 | 44%$^4\Sigma$+32%$^4\Delta$+22%$^4\Phi$ |
| (3)0.5 | 5194 | 5211 | 60%$^4\Pi$+30%$^4\Delta$+10%$^4\Sigma$ |

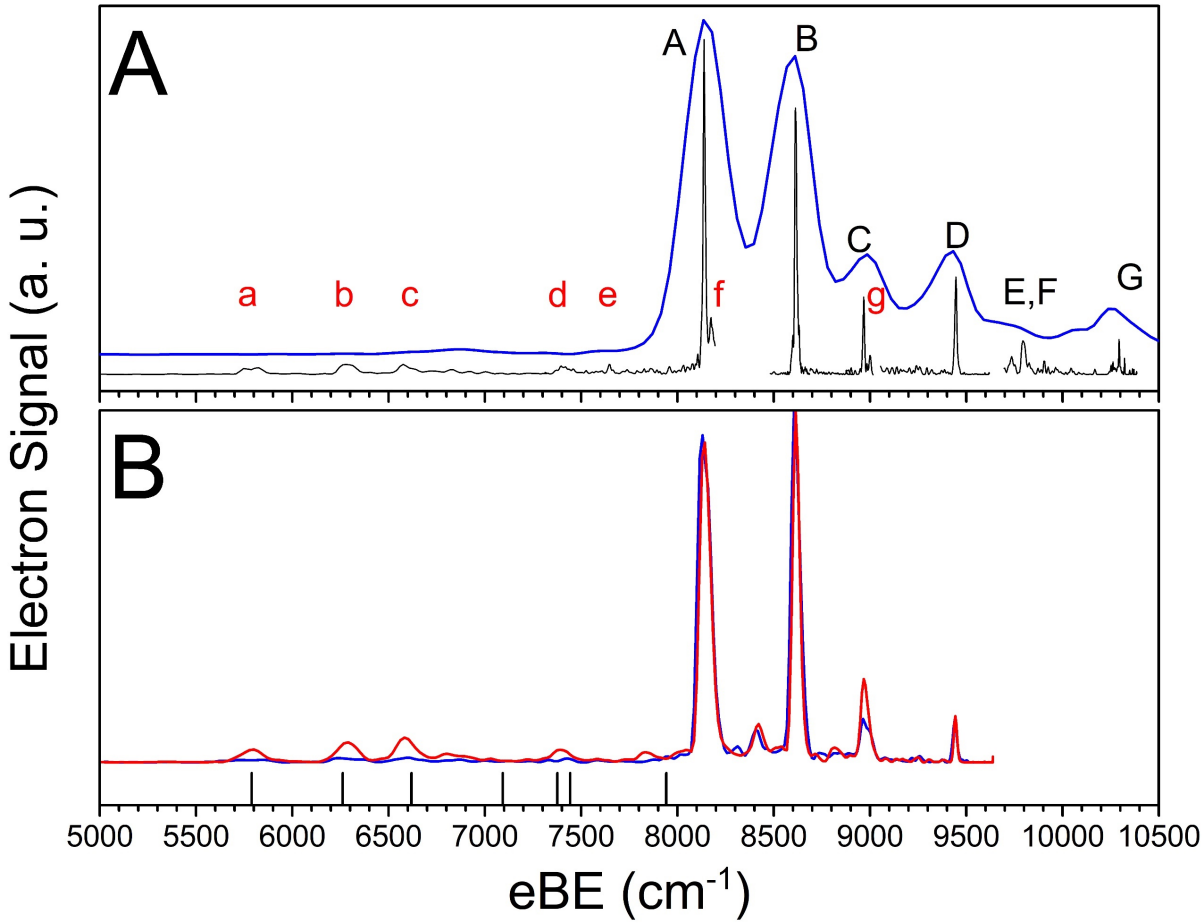


Figure 1. Low-eBE region of the cryo-SEVI spectrum of $NdO^-$. In A, the overview spectrum (blue, h$\nu$ = 15625 $cm^{-1}$) is vertically offset from the high-resolution scans (black, variable photon energies). Peaks labeled in red lower-case exhibit temperature-dependent intensities and are therefore considered hot bands. In B, buffer gas pressure in the trapping chamber is varied from low (red) to high (blue). Lower pressures lead to less efficient cooling in the trap and corresponding enhancement of hot bands. Below are black sticks corresponding to allowed detachment transitions from the (2)4.5 excited state of $NdO^-$ to known neutral levels of NdO as measured by Linton,[27] shifted in eBE by 2350 $cm^{-1}$ to simulate features a-e.

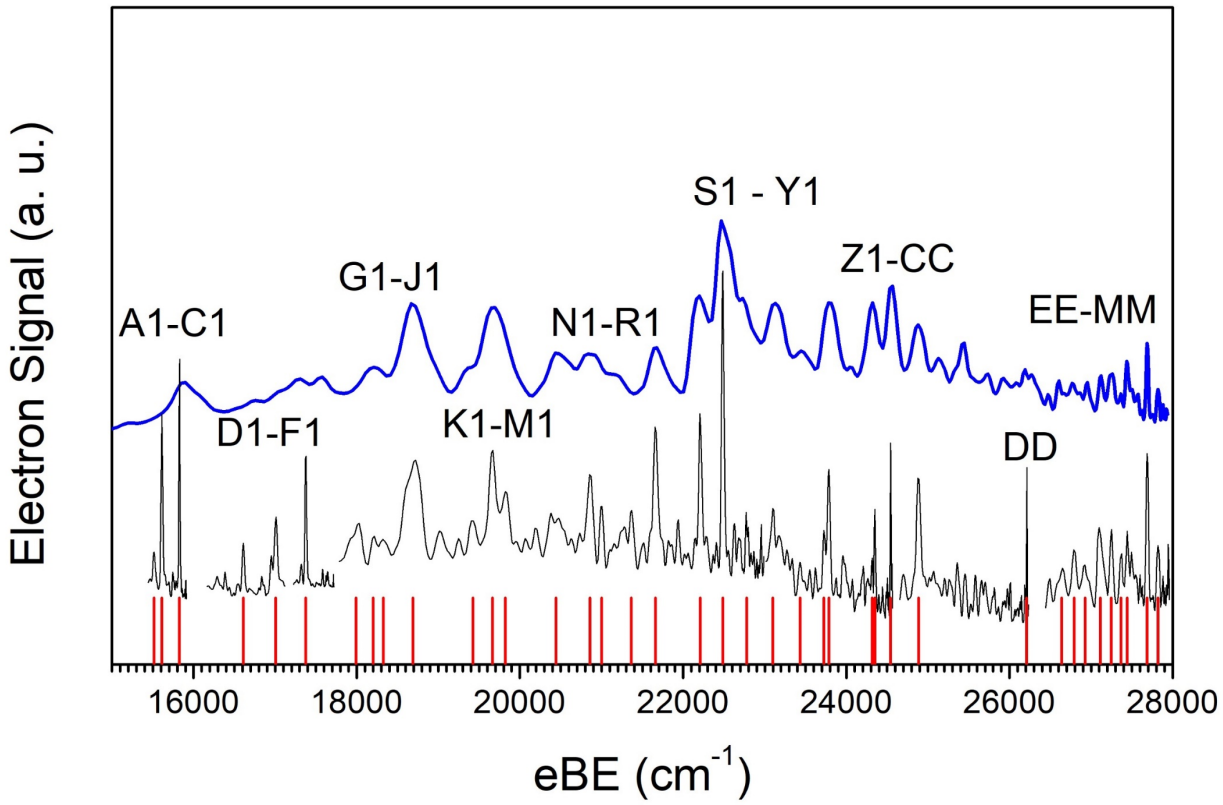


Figure 2. High-eBE region of the cryo-SEVI spectrum of $NdO^-$. The overview spectrum (blue, h$\nu$ = 27977 $cm^{-1}$) is vertically offset from the high-resolution scans (black, variable photon energies), peak centers for each transition listed in Table 2 are displayed (red sticks) for clarity.

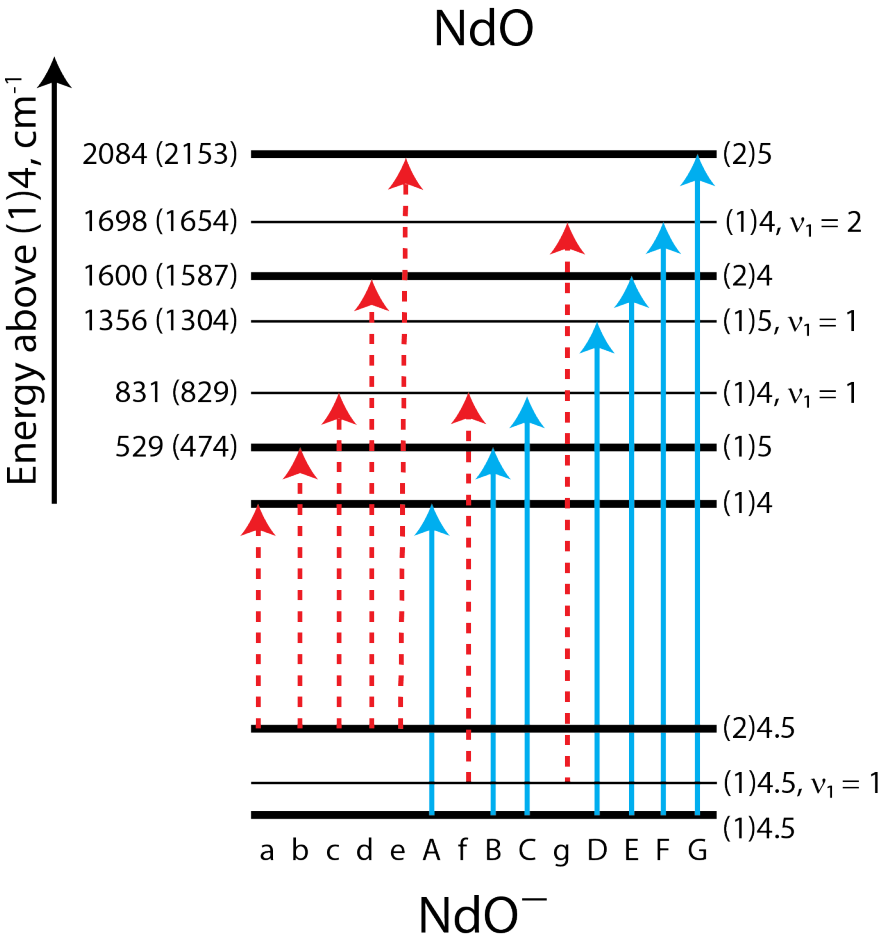


Figure 3. Energy level diagram of observed transitions from the (1)4.5 ground state (blue, solid lines) and proposed detachment from (2)4.5 excite state (red, dashed lines) of $NdO^-$ to various states of NdO in the low-eBE region (Fig. 1). Energies of states are reported both for our CASSCF calculations and those previously reported by Linton and coworkers,[27] in parentheses.